

Transient-Liquid-Phase Bonding of H230 Ni-Based Alloy Using Ni-P Interlayer: Microstructure and Mechanical Properties



MONICA KAPOOR, ÖMER N. DOĞAN, CASEY S. CARNEY,
RAJESH V. SARANAM, PATRICK MCNEFF, and BRIAN K. PAUL

Transient-liquid-phase bonding using Ni-P as an interlayer has been developed for H230 Ni-Cr-W solid-solution-strengthened Ni-based alloy. Two process parameters—composition of the interlayer and bonding time—have been varied to optimize the mechanical properties. H230 has been bonded into two sets of stacks (set I and II) for 8 and 4 hours using Ni-12P and Ni-6P interlayer, respectively, (wt pct) at 1423 K (1150 °C) and 12.7 MPa. The microstructure of both the stacks has three distinct regions—the joint centerline which showed the presence of pores, an isothermally solidified zone (ISZ) which did not have any carbide precipitates and base H230. Transmission electron microscopy and atom probe tomography showed a uniform microstructure, and an absence of any deleterious phases at the joint and in ISZ. Set I and set II had a yield strength of 76 and 86 pct of that of the H230 sheet, tested at 1023 K (750 °C). The measured elongation at fracture was negligible, but the fracture surfaces revealed a ductile cup-and-cone-type fracture occurring through the ISZ/joint region. Examination of broken tensile samples revealed that the plastic strain was constrained to within one joint region through which fracture occurred.

DOI: 10.1007/s11661-017-4127-5

© The Minerals, Metals & Materials Society and ASM International (outside the USA) 2017

I. INTRODUCTION

THE use of supercritical CO₂ (sCO₂) as a working fluid in power generation results in higher thermodynamic efficiencies compared to conventional power cycles that use steam as a working fluid.^[1,2] This high thermodynamic efficiency is in part due to the use of compact heat exchangers (CHX), which enhance heat transfer between the high- and low-temperature working fluid. One of the CHX designs features a microchannel architecture^[3] which is fabricated by joining multiple thin sheets which have microchannel design features machined in them. These sheets are then stacked and bonded together using a diffusion-based process such as transient-liquid-phase (TLP) bonding. A primary reason for using this joining process is its ability to yield tight dimensional tolerances for the microchannels, with

hydraulic diameters as small as a few hundred micrometers. Achieving tight dimensional tolerances in these microchannel HXs is critical to avoid pressure drop along the flow channels and thereby cause inefficiencies in operation.

These CHXs for sCO₂ applications typically operate at 20 to 30 MPa pressure differential between the hot and cold sides and up to 923 K to 1023 K (650 °C to 750 °C) on the hot side, with an anticipated lifetime of 30 years. These operating conditions whittle down the field of currently available candidate materials to a few Ni-based alloys. H230 is one such Ni-Cr-W-Mo solid-solution-strengthened Ni-based alloy which provides excellent creep resistance and oxidation properties near the operating temperature of these heat exchangers.^[4-6]

TLP bonding uses a coating on the joining surfaces, which acts an interlayer between the joining surfaces and has a lower melting point than the two surfaces which are being joined. This lower melting point is achieved by adding an element which acts as a melting point depressant (MPD), such as B, P, or Cr^[7-16] for joining Ni or Ni-based alloys. On heating up to the bonding temperature, the interlayer liquefies and the MPD diffuses into the base metal, lowering its melting point and resulting in the expansion of the liquid zone into the base alloy.^[17] Over time, this liquid zone

MONICA KAPOOR and ÖMER N. DOĞAN are with the National Energy Technology Laboratory, U.S. Dept. of Energy, 1450 Queen Ave SW, Albany, OR 97321. Contact e-mail: monica.kapoor@netl.doe.gov CASEY S. CARNEY is with National Energy Technology Laboratory, U.S. Dept. of Energy, and also with the AECOM, 1450 Queen Ave SW, Albany, OR 97321. RAJESH V. SARANAM, PATRICK MCNEFF, and BRIAN K. PAUL are with the School of Mechanical, Industrial and Manufacturing Engineering, Oregon State University, 204 Rogers Hall, Corvallis OR 97331.

Manuscript submitted February 9, 2017.

Article published online May 11, 2017

homogenizes to the equilibrium composition at the bonding temperature. As diffusion of MPD into the base alloy continues, the liquid zone begins to isothermally solidify forming a monolithic microstructure between the two surfaces to be joined. The solidification is driven by a change in composition at the bonding temperature due to diffusion of MPD into the base alloy.

The important TLP bonding process parameters which determine the quality (uniformity of microstructure) near the bond are bonding temperature,^[8,11,16,18,19] bonding time,^[7-9,15,18,20] the MPD used in the interlayer^[21] and its composition, width of the interlayer,^[15,19,20,22] etc. For instance, if the holding time at the bonding temperature is not long enough to result in complete isothermal solidification, a eutectic phase is formed at the bondline while cooling.^[7-9,15,18,20] Obviously, the formation of this eutectic phase detrimentally affects the ductility of the bond and is one of the primary challenges of this bonding process. Moreover, these process parameters are not independent and can interact to yield unexpected results, specially when multiple elements are present in the base alloys to be joined. A case in point is the diffusion rate of an MPD. On one hand, this diffusion rate will control the time needed for complete isothermal solidification to avoid the formation of brittle intermetallic phases. For instance, B diffuses faster than P in Ni, and therefore, the time required to complete the isothermal solidification will be shorter.^[12] On the other hand, rapid diffusion of B combined with its low solubility in Ni results in an oversaturation of B in the vicinity of the joint causing precipitation of borides.^[8] To summarize the above discussion, TLP bonding process-parameter-optimization for one combination of interlayer and base metal/alloy cannot be extrapolated to another combination and needs to be optimized using a combination of computational and experimental investigations.

Most of the current studies investigate either the microstructure using scanning/transmission electron microscopy (SEM/TEM)^[7,8,15,18,22] or the mechanical properties around the TLP bond or the joint.^[23] No studies focusing on relating the microstructure of the joints to its mechanical properties or on understanding the failure mechanisms in such joints were found. These types of studies are imperative if TLP bonding is to be used for practical long-term applications.

This study is a subset of a project to develop a heat exchanger prototype with a lifetime of ~30 years using TLP bonding for fabrication. Usually, long bonding times of TLP bonding are an impediment to its use in industry but given the relatively long lifetime of the heat exchanger, bonding time of a few hours is not a concern. TLP bonding has been studied extensively on Ni and even on various Ni-based superalloys,^[8,10,11,13,15,18,19] but there are very limited TLP bonding studies on H230 Ni-based alloy.^[24] The goal of this study was to obtain a high-quality uniform bond and perform tensile testing on it to understand its mechanical properties for use in the CHXs. Particularly, a Ni-P interlayer was used for TLP-bonding H230, and its effect on microstructure and the mechanical properties was studied.

II. EXPERIMENTAL PROCEDURES

A. TLP Bonding H230 Sheets: Bonding Setup and Parameters

H230 is a solid-solution-strengthened Ni-Cr-W-Mo-based alloy with excellent high-temperature strength and oxidation resistance. Details of the composition of H230 are provided in Table I. Solution-treated H230 was received as a sheet with approximately ~530 μm thickness. The sheet was cut into 14.5 cm^2 (2.25 in^2) cross-sectional sheets which were then plated with a 3- μm -thick Ni-P alloy to act as the low-melting interlayer. In case of alloys which form an oxide on the surface, a cleaning step is imperative before the coating is applied. If the surface is not cleaned, the coating will not adhere to the surface and eventually will not bond. The plated H230 sheets were then mounted onto a fixture and were bonded in vacuum ($<1.33 \times 10^{-8}$ MPa (10^{-5} Torr)) into stacks containing 100 sheets each, Figure 1.

1423 K (1150 $^{\circ}\text{C}$) is an optimal bonding temperature for H230 to balance diffusion processes to form the joint and to prevent excessive grain growth due to high temperature. A uniaxial pressure of 12.7 MPa was applied during the bonding to accelerate the bonding process. Additional details of bonding parameter selection are provided in Reference 25.

Two sets of parameters were studied in TLP bonding—composition of the interlayer and time required for bonding. Set I had Ni-12 wt pct P composition interlayer and was bonded for 8 hours. Set II had Ni-6 wt pct P interlayer composition and was bonded for 4 hours. To orient the readers to context of the Ni-P interlayer and H230 being TLP-bonded, a description of the TLP bonding process with the combination in set I is provided below with a Ni-P phase diagram, Figure 2.^[26] The inset in Figure 2 shows a close-up of the low-P (0 to 0.2 wt pct) region of the phase diagram.

The TLP bonding consists of three steps: (1) Melting of the interlayer, (2) Homogenization of the liquid, and (3) Isothermal solidification. Dissolution of the interlayer is very fast and usually occurs while the stacks are being heated up to the bonding temperature. In this case, as the stack is heated to 1423 K (1150 $^{\circ}\text{C}$), the interlayer will melt completely at ~1173 K (900 $^{\circ}\text{C}$) and will have a composition of 12 wt pct P. While heating up to 1423 K (1150 $^{\circ}\text{C}$) and holding at 1423 K (1150 $^{\circ}\text{C}$), P will diffuse into H230 and cause melting of the alloy layer adjacent to the liquid interlayer. This dissolution of H230 will eventually bring the composition to equilibrium composition C_L or point A in Figure 2, along the tie-line at 1423 K (1150 $^{\circ}\text{C}$).

The dissolution of H230 and the subsequent homogenization progressively lowers the net amount of P in the liquid and its composition will eventually stabilize at C_L or point A. Now, there is still a difference in the composition of P in the H230 and in the liquid region. Therefore, diffusion of P into the solid H230 will continue. However, further diffusion of P results in entering the two-phase region, and therefore, solidification will start at the bonding temperature and the region

Table I. Physical Properties of H230 and its Composition (Weight Percent) with Ni as Balance

Physical Properties											
Density						8.97 g/cc					
Melting Point						1574 K to 1644 K (1301 °C to 1371 °C)					
Composition											
Cr	W	Co	Mo	Fe	Mn	Si	Al	C	La	B	
22	14	5*	2	3*	0.5	0.4	0.3	0.10	0.02	0.015*	

*Maximum.



Fig. 1—H230 TLP-bonded stack and tensile testing specimens machined from the stack. The inset shows the H230 sheets before they are bonded.

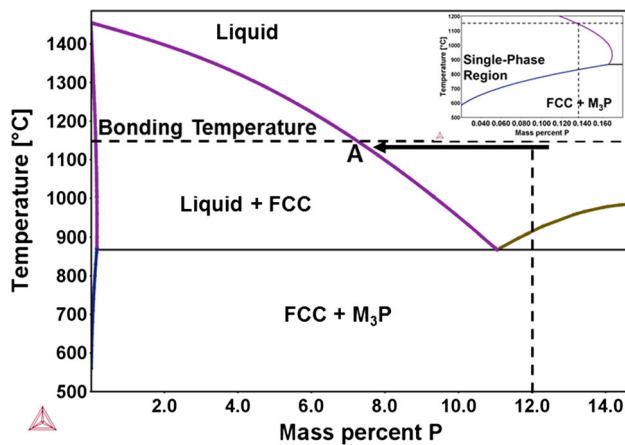


Fig. 2—Ni-P phase diagram with the vertical dashed line at the interlayer composition of set I at 12 wt pct. The inset shows a close-up of the low-P (0-0.2 wt pct P) region.

so formed is called the isothermally solidified zone (ISZ). This diffusion and solidification will continue till the liquid region solidifies and eventually homogenizes. However, if the bonding time is not enough for complete solidification, then cooling will result in a microstructure

depending on the composition of the liquid phase. Consequently, the microstructure near the joint center-line, which is the last to solidify, will have a eutectic composition, M_3P -based phase. For set II, at the bonding temperature of 1423 K (1150 °C), Ni-6 wt pct P composition lies in the two-phase region containing liquid and alpha solid solution, with the liquid comprising ~85 pct of the region. A similar process to set I will occur, but in this case, there is both a solid and a liquid region present initially.

As will be shown in results, bonding time of 8 hours was enough for complete homogenization of the bond in set I. Set II has a lower amount of P which diffused to a shorter distance, and therefore, the width of the liquid region was smaller, requiring a shorter time to homogenize. Consequently, the bonding time was reduced to 4 hours for set II.

Thermo-Calc 2015 was used for equilibrium thermodynamic and kinetic calculations using the database TCFE8.^[26] TCFE8 was used for all thermodynamic and kinetic calculations because mobility database of P in Ni is not available.

B. Structural Characterization

1. Analysis at the micrometer scale

Samples measuring approximately 10 mm × 5 mm were cut from the TLP-bonded stacks for microstructure characterization. These samples contained approximately 5 to 10 joint regions. The samples were mounted in conductive media and polished to 1 μm with a diamond suspension followed by an etch with $CuCl_2 + HCl + HNO_3$ for approximately 15 to 30 seconds to delineate the grain boundaries. SEM, to study the general microstructure and composition of the H230 sheet and the joint region, was performed at 20 KV on FEI Inspect F SEM. Area fraction of the precipitates is calculated from SEM images using Image J and it is assumed that the area fraction on the plane of observation is equivalent to a volume fraction.^[27] X-ray energy dispersive spectroscopy (EDS) composition analysis, to identify a composition gradient across the H230 sheet and joint region, was performed because H230 is a solid-solution-strengthened alloy and a composition gradient can alter its strength. Eventually, a composition difference can also result in a different corrosion response to the sCO_2 environment.

2. Analysis at the sub-micrometer scale: transmission electron microscopy and atom probe tomography

Transmission electron microscopy (TEM) studies were performed to identify the presence of any small phases near the bondline. TEM studies were performed using a 200 KeV Philips CM200 microscope. The TEM lamella, approximately $6\ \mu\text{m} \times 1\ \mu\text{m}$ in cross-section, were prepared using scanning electron microscope/focused ion beam (SEM/FIB) microscope Helios 650. The samples were lifted out from near the bondline to capture the interface, Figure 3(a). The TEM lamella which has been cut but not yet lifted out from the sample, Figure 3(b), shows an interface which is the TLP bondline along the middle of the lamella. The lift out and thinning was performed with 30 KV beam energy at currents in the range of 0.3 to 0.5 nA. A clean-up step, with 2 KV beam energy and 70 pA current, was performed to remove the surface damage due to Ga implantation.

Atom probe tomography (APT) was performed at the TLP bond, near the end of the ISZ region and in the middle of the sheet. The goal was to identify the presence of nanoscale phases in the vicinity of the bondline and to measure the composition. The studies were conducted using a Cameca local electrode atom probe (LEAP®) 4000 HR. APT tip blanks (approximately $1\ \mu\text{m}$ diameter) were prepared using Quanta 3D Dual Beam™ SEM/FIB microscope. The tip blanks were sharpened into a needle-like shape by annular ion milling followed by low-energy clean-up step to remove the surface damage due to Ga implantation. The APT

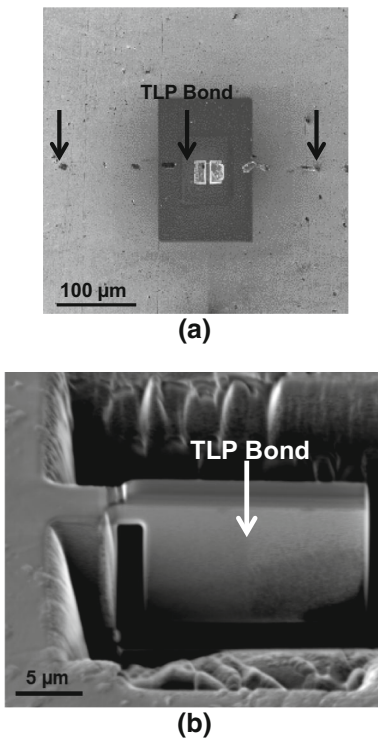


Fig. 3—(a) Region in the vicinity of the bondline showing the approximate position of the liftout, and (b) TEM lamella which has been cut (but not lifted out) and shows the TLP bond running through it.

studies were conducted in laser mode with a pulse repetition rate of 250 KHz and a pulse energy of 60 pJ at 40 K ($-233\ ^\circ\text{C}$) base temperature. The data were reconstructed using image visualization and analysis software (IVAS™) 3.6.12. All the runs were reconstructed using the voltage method and all the mass spectra were ranged at a bin size of 0.01 Dalton. Additionally, similar reconstruction parameters have been used for all reconstructions to ensure uniformity.

C. Mechanical Testing

Tensile tests were performed as specified in ASTM standard E8-13a^[28] in an Instron load frame. Solid cylindrical blank specimens were wire electrical-discharge-machined (EDM) from TLP-bonded stacks. The tensile specimens, gauge length of 22.86 mm (0.90 inch) and gauge diameter of 6.35 mm (0.250 inch), were machined from blanks such that the tensile loading was perpendicular to the bonding plane and along the short transverse direction of the H230 sheet (Figure 1). Tensile testing was performed at room temperature (RT) and at 1023 K (750 °C), which is close to the maximum operating temperature of these heat exchangers. Contacting extensometers were used to measure the sample strain at RT but the extensometers were removed at 1023 K (750 °C) due to slippage. The samples were preloaded to 0.10 kN and heated, in a clam shell-type resistance furnace, at 1023 K (750 °C) for 30 minutes before load application. Load was applied until failure on an electrically actuated load frame at a constant crosshead speed of 0.114 mm/min (0.004 inch/min). For tensile testing results of sheet H230 which has been obtained from Haynes technical data document, the application of load during tensile testing would be in a longitudinal or longitudinal-transverse direction. This is perpendicular to the direction in which load was applied during tensile testing in this study, *i.e.*, short transverse direction.

For the purpose of mechanical testing in this study, bulk H230 refers to 12.5-mm ($\frac{1}{2}$ in.)-thick plates and sheet H230 refers to 530- μm -thick sheets of H230 alloy.

III. EXPERIMENTAL RESULTS

A. Microstructure Characterization

To provide a perspective of the macrostructure of the TLP-bonded stack—sheet and the joint—Figure 4(a) shows a low magnification optical micrograph of cross-section of etched H230 TLPB stack-I. The joint regions (labeled with arrows) are clearly delineated at a periodicity of approximately $530\ \mu\text{m}$, which is consistent with the thickness of H230 sheets. A few pores are observed along the joint region which are thought to form due to solidification-related shrinkage. These are discussed in detail in the next section. Grain growth across the joint region, which is an indicator of a good quality joint is also observed, Figure 4(b).

Figure 5(a) shows a low- and Figure 5(b) shows a high-magnification SEM image (backscattered

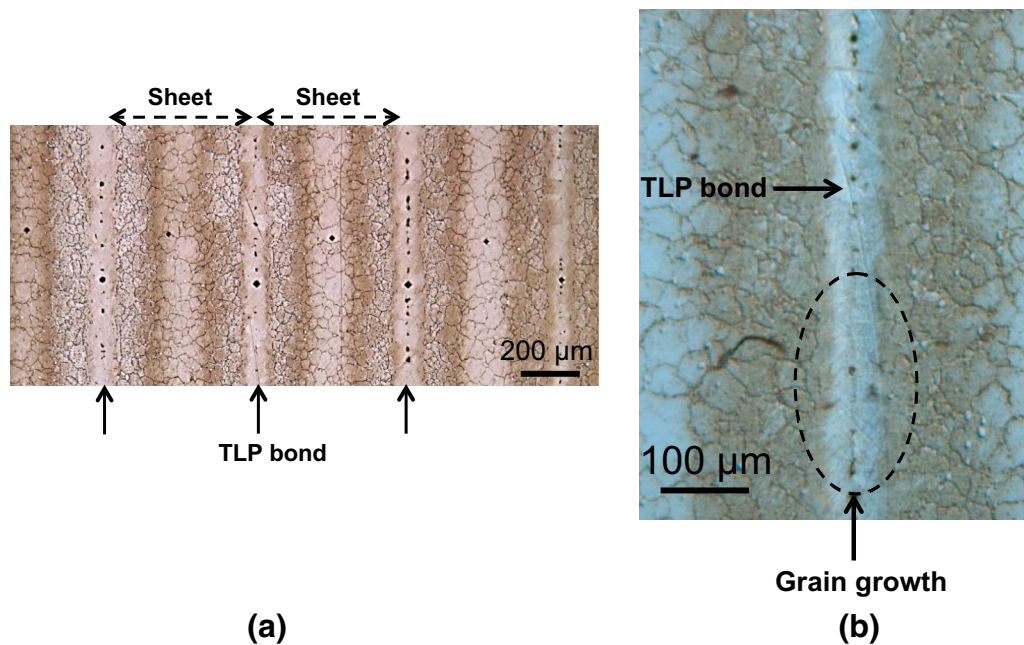


Fig. 4—Optical micrographs of etched H230 TLPB stack-I showing the (a) macrostructure and (b) microstructure of the sheet and the joints in the stack.

electrons) of the joint region. The low magnification image is to illustrate the uniformity across multiple joints. Three distinct regions are observed in the SEM image: (1) Joint centerline/TLP bond, (2) a region near the joint centerline, which is free of any precipitates as resolved by SEM, which is the isothermally solidified zone (ISZ), and (3) base H230 consisting of bright contrast precipitates (labeled as sheet). Focusing on the joints, multiple pores were observed coinciding with the location of the joint centerline. Such pores could be due to various reasons such as shrinkage^[29] while solidification, variable liquid front speed and large intermetallic grains^[22,30] increasing the roughness of the surfaces to be jointed. However, absence of any such intermetallic phases near the bondline in this study precludes pore formation due to increased surface roughness. A close-up of these pores, Figure 5(c), shows a lamellar microstructure on the pore walls formed due to eutectic solidification at least at the bondline suggesting that these pores could have formed due to solidification-related shrinkage. The lamellar microstructure on the pore walls suggests that there may still be enough P (>0.14 wt pct) at the locations solidifying last (pore walls on the bondline) to form the eutectic M_3P -based phase. This observation is also consistent with the thermodynamic calculations, Figure 2. The individual lamella on the pore walls are ~ 100 nm apart, which precluded the use of SEM to conclusively identify M_3P .

Second, the length of the ISZ, identified by the absence of bright precipitates, for set I is $\sim 48 \pm 7 \mu\text{m}$ and for set II is $44 \pm 6 \mu\text{m}$ from the joint centerline. The marginally smaller width of the ISZ in Set II can be explained by the lower amount of P in the interlayer. This lower amount of P indicates that while heating to bonding temperature, P needs to diffuse to a shorter distance into the base metal to establish equilibrium,

and therefore, a smaller width of the base alloy will be liquid by the time bonding temperature is reached. Since complete isothermal solidification (except at the walls of the pores) was observed in both set I and set II, it is surmised that the difference in bonding time was not a dominant factor in this case. Even though many other studies on the effect of bonding time^[7,9,10,18,31] on the width of ISZ have shown a direct relation between the width of the ISZ and the bonding time, those studies looked at shorter times, less than 2 hours. In this study, the shorter time of 4 hours is also enough to complete the isothermal solidification, and therefore, bonding time is not a dominant factor.

The bright precipitates in the base alloy contained W and Mo as seen in EDS maps, Figure 6. Spot EDS obtained from these precipitates indicated the presence of W (58.2 ± 2.3 wt pct), Mo (5.5 ± 0.3 wt pct), Cr (12.9 ± 0.3 wt pct) and also Ni (18.6 ± 0.5 wt pct) in the precipitate. Equilibrium thermodynamic calculations also predict that these precipitates will contain ~ 15 wt pct Ni and 10 wt pct Cr, but the respective EDS maps did not show any enrichment probably due to the relatively low amount in the precipitates compared to the matrix. Such precipitates containing W, Mo and Ni have been very well characterized in H230 alloy and are known to be of M_6C -type.^[5,6] These M_6C -type precipitates had a volume fraction of approximately 5.59 and 2.05 pct in Set I and set II, respectively. The volume fraction was calculated considering only the region which contained the precipitates and excluded the ISZ. The higher volume fraction in Set I can be explained by almost double the bonding time used for Set I, which provided the precipitates more time to grow. The EDS maps also show a few smaller Cr-rich precipitates nucleating along grain boundaries. These have been identified as the secondary $M_{23}C_6$ precipitates, which

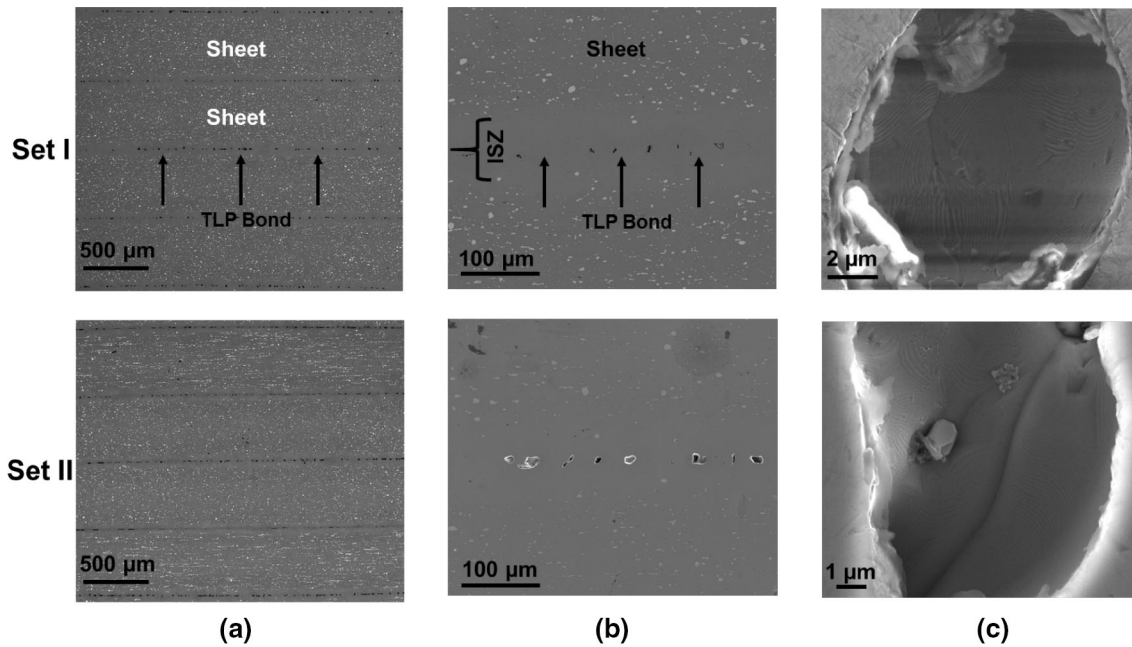


Fig. 5—Backscattered electron (BSE) SEM images of H230 TLPB stacks showing the (a) macrostructure and (b) the microstructure in the vicinity of the bond region, and (c) secondary electron (SE) SEM images showing the close-up of the pores at the bondline.

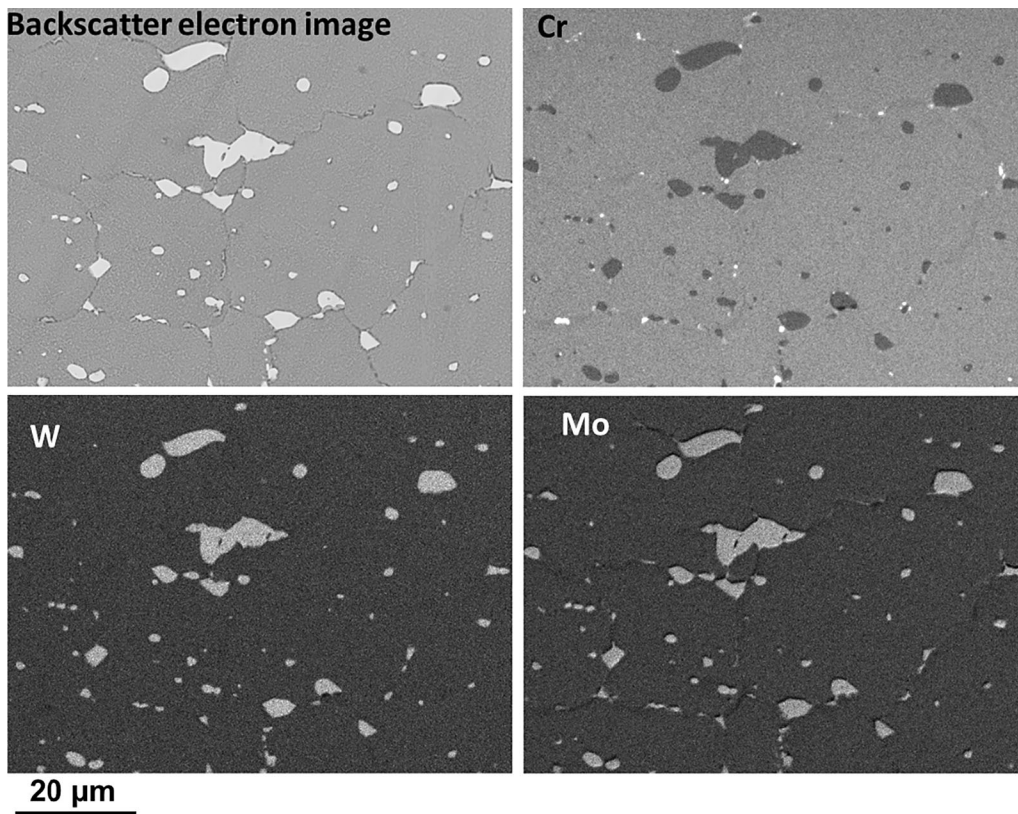


Fig. 6—EDS maps from a region adjacent to the isothermally solidified zone showing that primary precipitates are rich in W and Mo.

preferentially nucleate at grain boundaries, dislocations or twin boundaries and are partially responsible for the excellent creep properties of H230.^[5] These secondary precipitates are not predicted to form at the bonding

temperature. However, their presence suggests that they could have formed after the bonding process was finished and the stacks were cooled down to room temperature at .033 K/sec (2 °C/min).

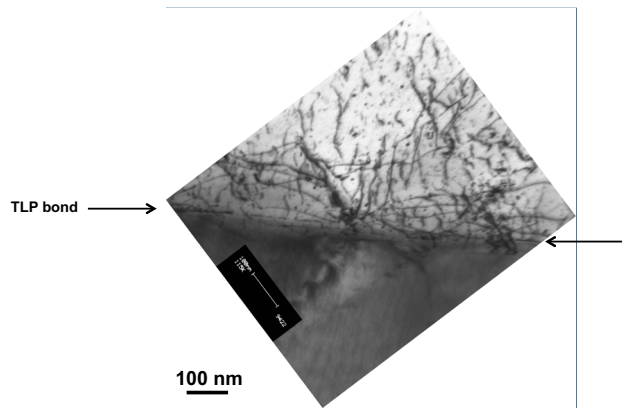


Fig. 7—TEM image of the TLP bondline showing two different grains on each side.

ISZ near the joint centerline did not have any M_6C -type of precipitates that could be resolved by SEM. Therefore, TEM analysis was performed on a region near the bondline, and it showed a uniform microstructure without the presence of any M_6C -type precipitates near the bondline, Figure 7.

Similarly, APT was performed at three regions: (1) at the bondline, (2) at the end of ISZ, *i.e.*, the boundary between the ISZ and the base alloy, and (3) in the middle of the sheet—to study the uniformity of the microstructure. Figure 8 shows atom maps of (a) Ni, (b) Cr, (c) W, and (d) P from the ISZ obtained using APT. There is no evidence of any P-based intermetallic formation (M_3P) or precipitate formation or clustering, even at the nanoscale. These results indicate a uniform microstructure in the ISZ.

Since APT has an equal analytical sensitivity for all elements of up to 1 atomic parts per million, it allows accurate quantification of composition of even light elements such as C and/or elements present in low amounts such as P in this alloy.^[32,33] Since these experiments are challenging and arduous to perform, composition analysis as a function of distance from the joint centerline was performed at three points—at the bond line, at the end of ISZ, and in the middle of the sheet (approximately 275 μm away from the joint).

Studying the composition distribution is important because the interlayer has only Ni and P and the alloy H230 also has Cr and W as its main constituents. Therefore, when the sheets are bonded at 1423 K (1150 $^{\circ}\text{C}$), Ni and P will diffuse into H230 and Cr, W and other constituents will diffuse into the interlayer for homogenization. After bonding it is important to understand the distribution of the elements that provide: (1) solid-solution-strengthening, (2) oxidation resistance to the alloy, and (3) composition of P (MPD) which may form M_3P -based intermetallics. Moreover, even though there is no conclusive evidence on the effect of P on the properties of H230, the industry specification recommends keeping it below 0.02 wt pct.^[34,35]

Figures 8(e) through (g) show composition of W and Cr; Ni; and P and C, respectively, dissolved in the matrix as a function of distance from joint centerline, as determined by APT. The error bars were not shown in

the charts because they were smaller than the data markers. Details of composition with the standard deviations (in wt pct) are listed in Table II. There is 12.37 ± 0.02 W near the joint which increases to 12.72 ± 0.03 at the end of ISZ and decreases to 12.37 ± 0.02 at the middle of the sheet. Cr dropped to 19.44 ± 0.01 near the joint, whereas it was 22.87 ± 0.02 in the sheet and Ni composition dropped from 64.01 ± 0.03 near the joint to 63.50 ± 0.04 in the middle of the sheet. P composition changes from 0.19 ± 0.001 to 0.012 ± 0.003 in the middle of the sheet. Last, C composition changes from 0.0094 ± 0.0001 at the joint to 0.0252 ± 0.0002 in the middle of the sheet.

A similar composition analysis using SEM EDS was performed at an interval of approximately 50 μm from joint centerline to the middle of the sheet. Each reading is an average of ten measurements and the goal was to balance the accuracy of the localized APT composition measurements with composition measurements performed over a much larger area. Figures 9(a) through (d) show composition of W, Cr, Ni, and P dissolved in the matrix as a function of distance from joint centerline to the middle of the sheet. The filled symbols are from set I and show that W composition profile is relatively flat and almost unchanged from 12.5 ± 0.2 near the joint to 12.3 ± 0.2 in the sheet. Cr dropped to 18.7 ± 0.2 near the joint, whereas it was 22.5 ± 0.2 in the sheet. Ni composition dropped from 65.4 ± 0.3 near the joint to 61.9 ± 0.2 in the middle of the sheet, and P changes from 0.35 ± 0.05 to 0.06 ± 0.08 (wt pct).

The empty symbols are from set II and also show similar compositions except for P (0.21 ± 0.05 near the centerline to 0.06 ± 0.07 in the sheet) and W (12.24 ± 0.5 near the bondline and 13.34 ± 0.3 in the middle of the sheet). The difference in P composition between set I and set II can be explained by difference in Ni-P interlayer composition—12 and 6 wt pct P in set I and II, respectively. The difference in W composition can be attributed to a couple of factors as follows. W is a heavy element and would be the slowest to diffuse in H230. Therefore, it stands to reason that the difference in bonding time between set I (8 hours) and set II (4 hours) will impact W diffusion the most. This effect is reflected in the relatively flatter composition profile of set I. C measurements with EDS are not plotted because of the inaccuracy associated with light element composition measurement in SEM EDS.^[36] An interesting point to note is that localized APT composition measurements are consistent with EDS composition measurements.

Regardless, no deleterious phases were noted in SEM studies of set I and set II.

B. Mechanical Property Testing

1. Set I

On testing at room temperature (RT), yield strength of TLP-bonded stack (382 ± 3 MPa) was 90 pct of that of the H230 sheet (422 MPa). On testing at 1023 K (750 $^{\circ}\text{C}$), which is close to the operating temperature of the heat exchanger, the yield strength of TLP-bonded stack (245 MPa) was 76 pct of the H230 sheet (323 MPa). Details of mechanical properties are summarized

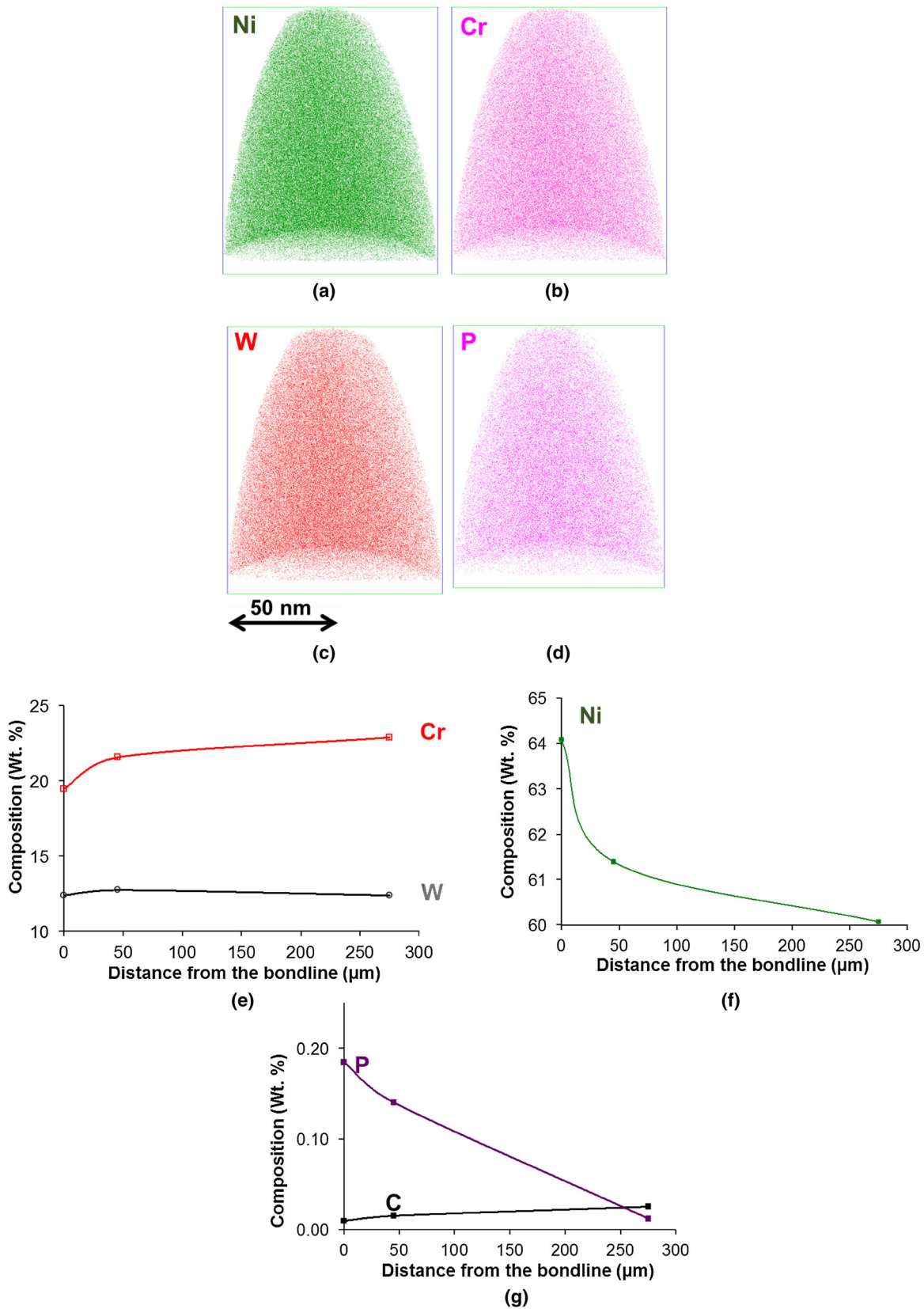


Fig. 8—Atom maps of (a) Nickel, (b) Chromium, (c) Tungsten, and (d) Phosphorus obtained from APT of ISZ of set I stacks to illustrate the absence of any second phases. Composition profiles as a function of distance from the joint of—(e) Cr and W, (f) Ni, and (g) P and C. The composition is obtained by APT measurements. The error bars are smaller than the data markers and are provided in Table II.

Table II. Compositions (Weight Percent) of Ni, Cr, W, C, and P Obtained from the Bondline, the End of ISZ and the Middle of the Sheet Using APT

	Ni	Cr	W	C	P
Bondline	64.01 ± .03	19.44 ± 0.01	12.37 ± 0.02	0.009 ± 0.0001	0.19 ± 0.001
End of ISZ	61.39 ± 0.04	21.55 ± 0.02	12.72 ± 0.03	0.015 ± 0.0002	0.14 ± 0.001
Middle of the Sheet	60.07 ± 0.04	22.87 ± 0.02	12.37 ± 0.02	0.025 ± 0.0002	0.012 ± 0.0002

The error of each concentration measurement $\sigma = (c*(1 - c)/N)^{1/2}$.

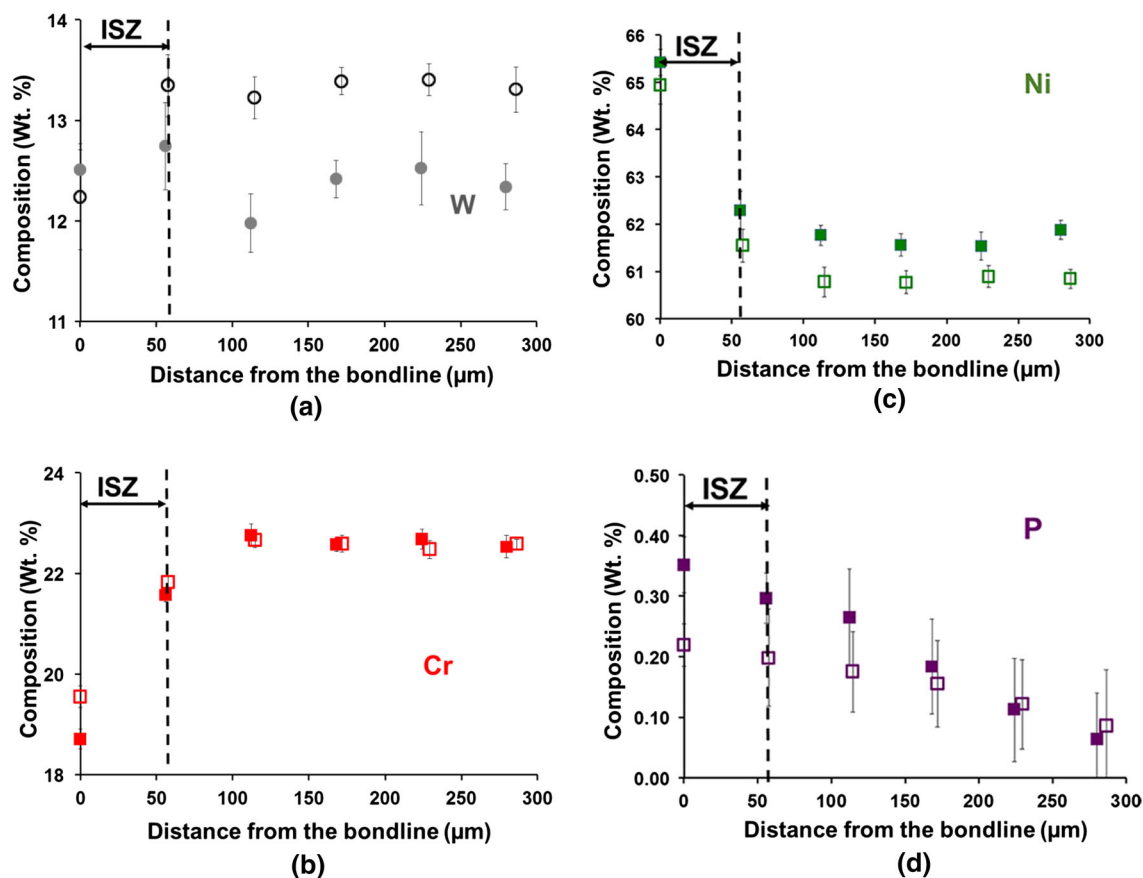


Fig. 9—EDS composition profiles as a function of distance from the joint of—(a) W, (b) Cr (c) Ni, and (d) P. The filled and empty symbols are from set I and set II, respectively.

in Table III. The fracture surfaces of the samples tested at RT appear flat at the macroscale, Figure 10(a). However, there was indisputable evidence of ductility at the microscale with a classic cup-and-cone appearance throughout the fracture surface, Figures 10(b) and (c). Linking the flatness at the macroscale and ductility at the microscale suggests that the fracture is occurring through the narrow joint region and not through the sheet material. Additionally, the absence of precipitates (present only in the base alloy and not in the vicinity of the joint) at the fracture surface also indicates that the fracture is indeed occurring in the vicinity of joint region. The fracture surface of the samples tested at 1023 K (750 °C) appears flat at the macroscale, Figure 10(d). The topography of the surface indicates that it fractured through both the sheet and the joint

region. The fracture through the joint region again shows classical signs of ductility, Figures 10(e) and (f).

2. Set II

An additional heat treatment at 1473 K (1200 °C) was performed on set II in an effort to increase the strength. To distinguish it from the stack with no heat treatment, this stack will be designated set II-HT. The higher heat treatment temperature would serve two purposes: (1) dissolve some of the M_6C -type precipitates and free the solid-solution-strengthening elements, and (2) homogenize the composition between the ISZ and the sheet. The heat treatment temperature was obtained from Thermo-Calc® which predicted a lower volume fraction of these precipitates at 1473 K (1200 °C) than at 1423 K (1150 °C) (which was the bonding temperature).

Table III. Summary of Mechanical Properties of TLPB H230—Set I and Set II, and H230 Sheet (Cold Rolled) Tested at Room Temperature and at 1023 K (750 °C)

	Yield Strength (MPa)	Ultimate Tensile Strength (MPa)	Ductility Elongation (%)
Room Temperature			
TLP B H230-Set I-AR	382 ± 3	691 ± 2	14.0
H230 sheet-AR*	422	838	47.2
1023 K (750 °C)			
TLPB H230 Set I-AR	245	281	1.0
TLPB H230 Set II-AR	256 ± 1.3	261 ± 1.70	0.25 ± 0.2
TLPB H230 HT-ed Set II	278 ± 0.1	324 ± 3	0.75 ± 0.1
H230 sheet-AR*	323	539	61.2
Bulk H230-HT-I	235	380	121.8
Bulk H230-HT-II	253 ± 11	384 ± 1.76	42 ± 3

The error for each measurement is one standard deviation.

*Technical data document.

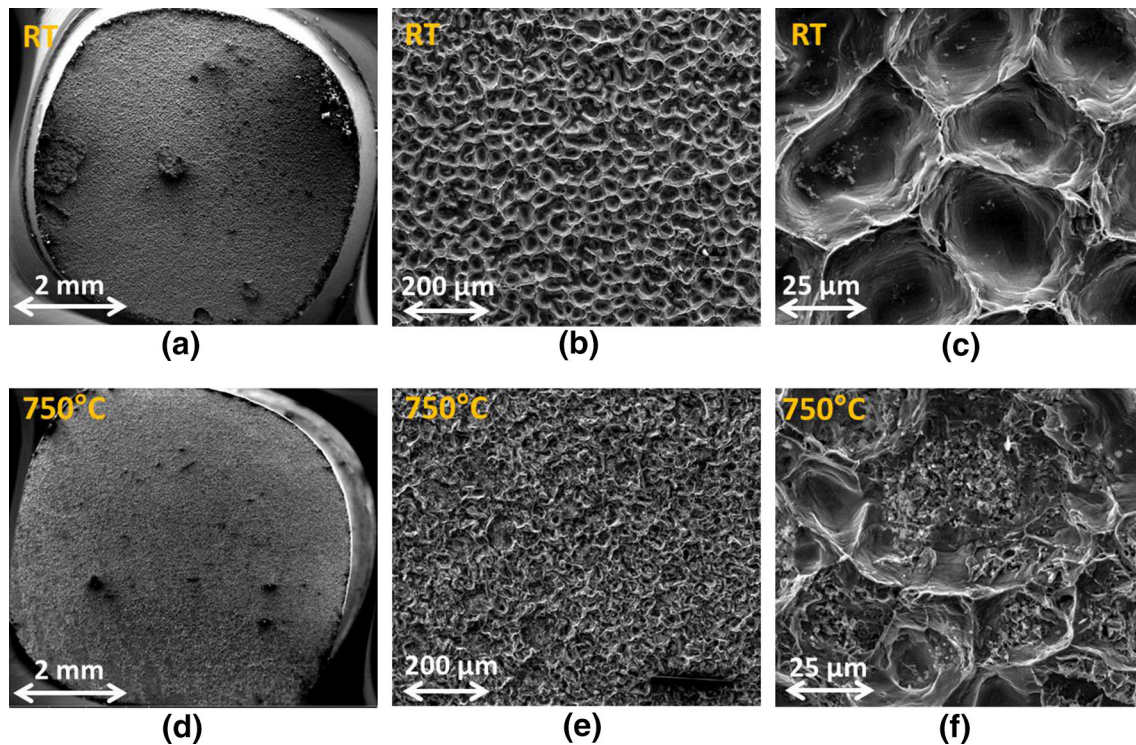


Fig. 10—(a) through (c) SEM images of the fracture surfaces of samples tested at RT, and (d) through (f) SEM images of the fracture surfaces of samples tested at 1023 K (750 °C).

To provide a comparison with bulk H230, as-received H230 ½ in thick plates (cut into rectangular tensile sample blanks) were heat treated to simulate the conditions of: (1) TLP bonding for set II (designated Bulk-HT-1), and (2) TLP bonding plus heat treatment (designated Bulk-HT-II). Due to the limited number of tensile samples available, the testing was performed only at the temperature of interest, 1023 K (750 °C), for the heat exchanger application.

The following two results are of note: (1) TLP-bonded stacks from Set I-AR, Set II-AR, and HT-ed set II have a yield strength which is 76, 81, and 86 pct, respectively, of the H230 sheet. (2) Comparing the yield

strengths of TLP-bonded stacks in Set II to the bulk H230 which has received analogous heat treatment to simulate the bonding condition, Set II-AR stack and Set-II-HT stack have a yield strength which is 111 and 107 pct of Bulk-HT-1 and Bulk HT-II. Details of the mechanical properties are summarized in Table III.

IV. DISCUSSION

TLP bonding of Ni-based alloy coated with Ni-P interlayer was performed to fabricate a microchannel heat exchanger. Two processing parameters—composition of

the interlayer and the time needed to bond were varied resulting in two sets of TLP-bonded stacks that were optimized for the final selection to fabricate the heat exchanger. Temperature and pressure required to bond were not varied.

TLP bonding resulted in two sets of stacks (Figure 1)—set I and set II—both of which had three distinct microstructural features (Figure 5): (1) the joint which did not have any deleterious phases present but had pores, (2) ISZ which solidified at the bonding temperature due to a change in composition driven by diffusion of P into the base alloy, and (3) the sheet zone which has a microstructure similar to the base alloy. Discussing the above features individually, presence of the pores at the bondline is a concern for long-term mechanical stability of the heat exchanger. The lamellar microstructure on the pore walls is consistent with the experimentally obtained P composition in Figure 9(d). P composition near the bondline is 0.20 wt pct and at this composition, the phase diagram in Figure 2 indicates the formation of a eutectic M_3P -based phase on cooling. Moving away from the bondline to the middle of the sheet, P composition drops to <0.14 wt pct, which is below the solidus line and would therefore not result in the formation of any M_3P -based phase.

Additional Scheil calculations conducted in Thermo-Calc show that 0.22 wt pct P (set II) at the bondline will result in ~1.8 wt pct of the solid being a M_3P eutectic phase near the bondline, Figure 11. This phase will form near the end of the solidification process, and since the bondline will be the last to solidify, these pores most likely are the result of solidification shrinkage. Set I also has similar results with only one difference—the calculated amount of eutectic phase is slightly higher, which can be explained by the higher amount of P near the bondline, Figure 9(d).

A general approach to eliminating the eutectic phases is to increase the bonding time. This increased bonding time helps the MPD diffuse into the base metal and thereby avoid the formation of eutectic phases. For both set I and set II, increasing the bonding time may not be effective. Set II numbers will be used for this discussion because it has a lower amount of P to begin with and it would be easier to eliminate the eutectic at the bondline. Set II has 0.22 wt pct P near the bondline and 0.09 wt pct P in the middle of the sheet. If the bonding time is increased and the P is allowed to diffuse into the base metal, the diffusion profile of P will flatten till there is equal amount of P near the bondline and in the middle of the sheet, approximately 0.15 wt pct. However, this amount of P is not low enough to eliminate the eutectic formation completely. Based on Thermo-Calc, to eliminate the formation of eutectic, the amount of P needs to be lower than 0.09 wt pct.

Moving to the ISZ, this region is characterized by the absence of carbide particles, which may reduce the strength of these bonded stacks because these particles pin the grain boundaries and retard grain growth. To understand the absence of M_6C -type precipitates in ISZ near the joint centerline, the heat treatment history of H230 sheets and results of equilibrium thermodynamic calculations are discussed as follows.

Commercial solution treatment of H230 at approximately 1523 K (1250 °C) results in the formation of the M_6C -type precipitates. After the completion of this step and the formation of these M_6C -type precipitates, Thermo-Calc predicts 2.6 pct precipitated volume fraction of M_6C -type precipitates and approximately 0.03 pct C and 11.7 pct W (wt pct) dissolved in the matrix. These calculated composition values are very close to the experimentally measured values—12.37 pct W and 0.025 pct C (wt pct) in the sheet in set I stack.

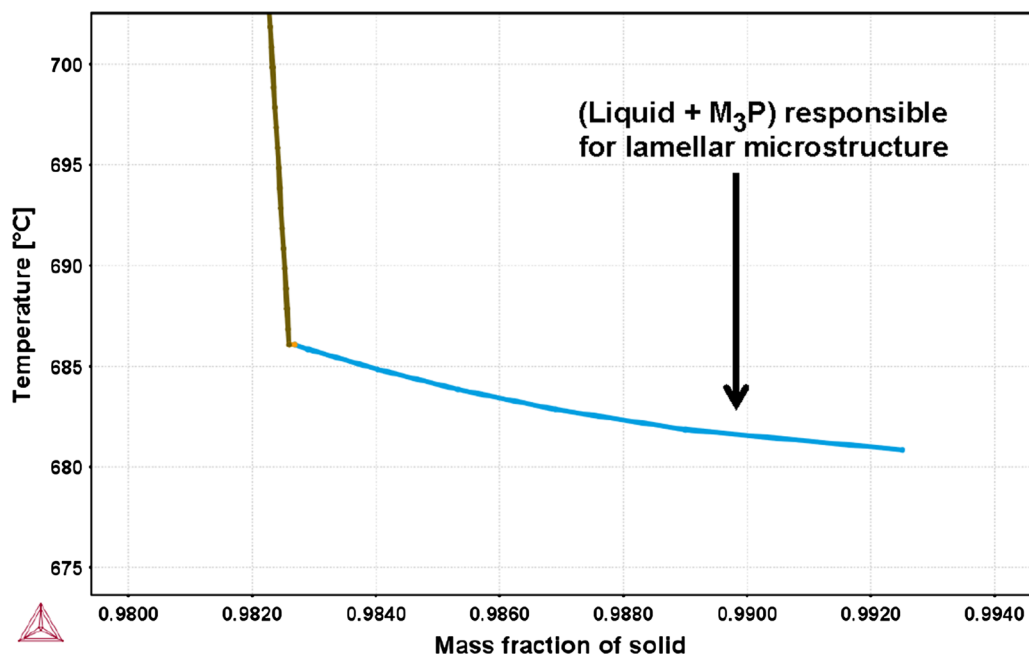


Fig. 11—Scheil calculation showing that the 0.2 wt pct P results in 1.8 wt pct of the microstructure consisting of liquid and M_3P phases.

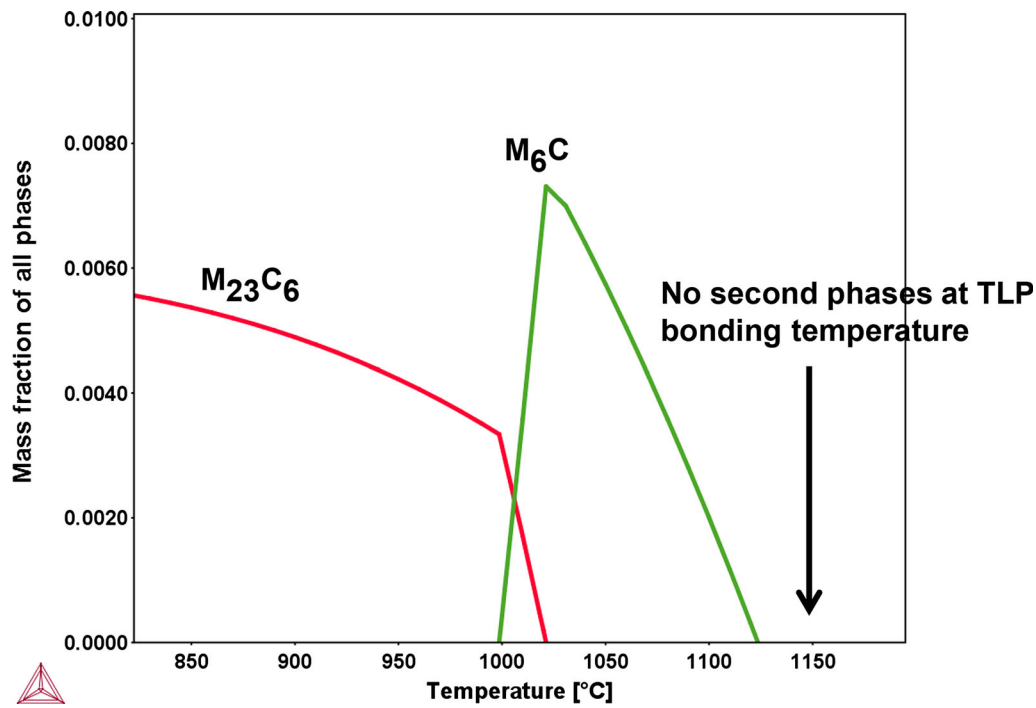


Fig. 12—Equilibrium mass fraction of phases as a function of temperature showing that no precipitate forms at the bonding temperature of 1423 K (1150 °C) in the ISZ.

After this step, Ni plating is applied to sheets and subsequently the sheet stacks are held at 1423 K (1150 °C) for 8 hours for TLP bonding. During this bonding process, Ni and P from the Ni-P interlayer will diffuse into the base alloy resulting in a net Ni enrichment in the vicinity of the interlayer. Similarly, elements from the H230 sheet will diffuse into the Ni-P interlayer and homogenize the composition. The matrix has approximately 0.03 wt pct C dissolved in it and even if it is assumed that 0.03 wt pct C diffuses into the Ni-P interlayer, this C and W amount is not high enough to form any precipitates at 1423 K (1150 °C), Figure 12.

The tensile samples were machined from the stacks such that the applied load is perpendicular to the broad faces (along the short transverse direction) of the H230 sheet and the ISZ/joint region. In such a case, the stress experienced by the two distinct features—H230 sheet and ISZ—is same, but the strains experienced by the two features will vary.^[37] On application of load, the softer joint region is constrained by the base alloy from deforming plastically, which sets up secondary tensile stresses at the joint/base alloy interface.^[37] As the applied load increases, this causes either the joint to fracture or to delaminate at the interface, which is consistent with the observed fracture surfaces of this study. Consequently, the measured properties in such a tensile test are those of the ISZ/joint region.

The RT measured yield strength of the sheet and set I is 422 and 382 MPa, respectively, *i.e.*, the TLPB stack has approximately 10 pct (40 MPa) lower yield strength than the sheet. Considering that the measured yield strength of set I reflects the strength of the joint/ISZ region, the ISZ is ~10 pct weaker than the base alloy. Therefore, contributions from various strengthening

mechanisms—solid-solution-strengthening, Hall-Petch strengthening, and Orowan strengthening—were quantified to understand the difference between ISZ and sheet. Solid-solution-strengthening and Hall-Petch strengthening result in an increase of 23 and 3 MPa, respectively, in the sheet. Orowan strengthening does not provide any strengthening in the sheet. Therefore, the additional difference (~15 MPa) could be due to: (1) difference in dislocation density in the sheet and the joint, (2) a rule-of-mixture-type hardening due to the presence of a harder carbide phase in the sheet, and (3) presence of pores along the joint centerline.

At 1023 K (750 °C), set I and set II had a yield strength of 76 and 81 pct compared to the bulk H230 sheet (Table III). Since set II had a higher yield strength, an additional heat treatment was performed on set II, which increased the yield strength to 86 pct of the H230 sheet. The low measured failure-to-elongation (compared to bulk H230), Table III, in the context of the ductile fracture surface suggests that the plastic strain is localized to the approximately 85 to 95 μm joint regions (weaker regions) and is not being transferred uniformly from the joint region to the sheet region throughout the gage section. Therefore, the measured value of elongation-to-failure which is traditionally normalized over the entire length of the gage section (and not just the joint where the elongation is occurring) can be misleading in this case. The length of the joint regions in this discussion is taken as a range to include set I, set II, and HT-ed set II joint regions.

This phenomenon of localized plastic strain is observed experimentally in SEM images of the curved surface, perpendicular to the fracture surface, of a fractured tensile sample. Figure 13(a) shows that the ISZ/joint layer 1

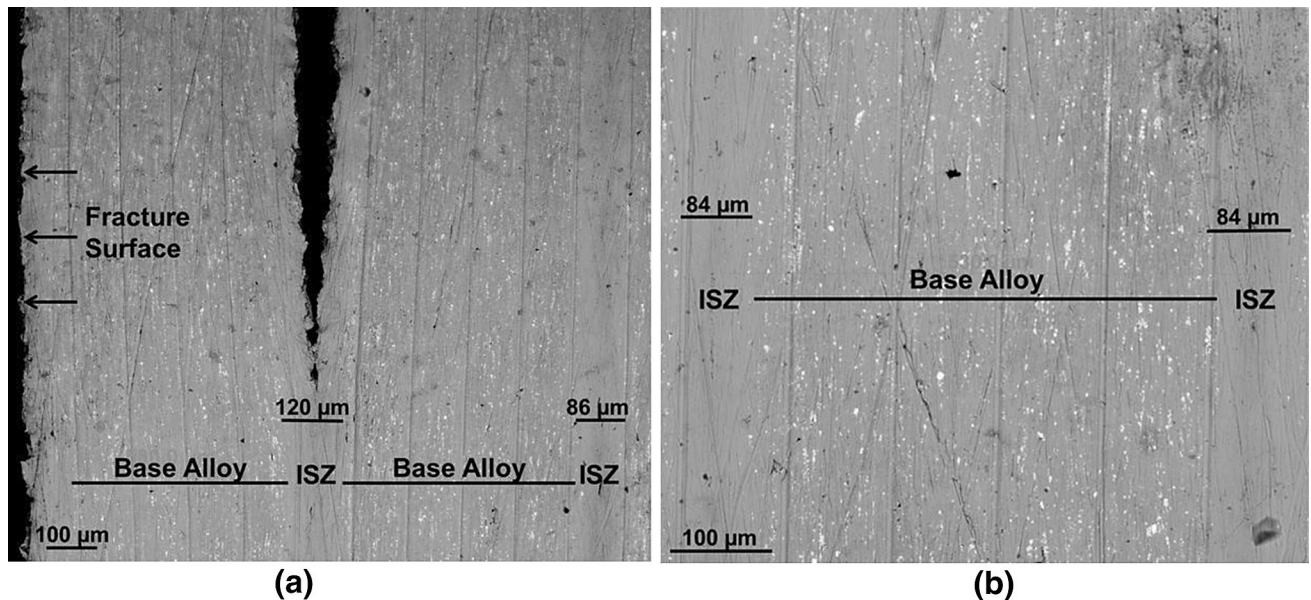


Fig. 13—The curved surface of a fractured tensile sample perpendicular to the fracture surface of TLP-set II-AR showing the region (a) adjacent to the fracture surface and (b) 10 layers away from the fracture surface. This sample was tested at 1023 K (750 °C).

adjacent to the fracture surface measures 120 μm but the ISZ/joint layer 2 adjacent to it, *i.e.*, second layer from the fracture surface measures 86 μm . This length of the ISZ layer 2 is equal to the ISZ length ($88 \pm 12 \mu\text{m}$) in the corresponding stack before fracture. This observation confirms that there is no transfer of strain beyond the second layer from the fracture surface during the application of load in a tensile test. Figure 13(b) shows a region which is ten layers away from the fracture surface and the ISZ/joint layer measures approximately 84 μm . In a nutshell, the elongation is limited to the layer which fractures and the adjacent layer, and therefore, conventional method of calculating elongation-to-failure would not be useful here. Calculating the elongation-to-failure based on just length of the elongated ISZ layer adjacent to the fracture surface, the elongation-to-failure of ISZ is approximately 38 pct.

V. CONCLUSIONS

1. H230 with Ni-12P (wt pct) as an interlayer was successfully TLP bonded with high-temperature yield strength approximately 76 pct of that of the H230 sheet.
2. H230 with Ni-6P (wt pct) as an interlayer was successfully TLP bonded followed by a heat treatment and had a high-temperature yield strength approximately 86 pct of that of the H230 sheet.
3. In both cases, the fracture occurs through the ISZ with classic cup-and-cone fracture surfaces. However, there was hardly any elongation measured at the macroscale. It is believed that the strain is constrained to a few bonds in the vicinity of fractured bond and is not transferred uniformly along the entire gage length.
4. The measured RT yield strength of the TLP-bonded stack is measuring the strength of the ISZ/joint region.

5. TLP-bonded H230 did not show the presence of any deleterious second phases near the bondline. The microstructure of the stack has predominantly three regions: (1) bondline, (2) isothermally solidified zone which extends about 45 μm average from the bondline in each direction, and (3) the sheet which has a microstructure similar to the base alloy.
6. ISZ does not have any carbide particles forming in it and equilibrium thermodynamic calculations indicate that there is not enough alloying elements (W and C) in the ISZ to nucleate carbide precipitates.
7. The walls of the pores forming at the bondline have a lamellar microstructure and are believed to form due to shrinkage while the bondline solidifies.

ACKNOWLEDGMENTS

This work was performed in support of the U.S. Department of Energy's Fossil Energy (FE) Advanced Turbines and Crosscutting Technology Research Programs and Energy Efficiency and Renewable Energy (EERE) Sunshot Program. This research was supported in part by an appointment (MK) to the National Energy Technology Laboratory Research Participation Program sponsored by the U.S. Department of Energy and administered by the Oak Ridge Institute for Science and Education. The authors would like to thank Christopher Powell for performing the tensile tests. The authors would like to acknowledge Haynes International (Dr. Vinay Deodeshmukh) for providing H230 Ni-based alloy and for the technical discussions on the physical metallurgy of H230. Atom probe tomography was performed using EMSL, a DOE Office of Science User Facility sponsored by

the Office of Biological and Environmental Research. MK is appreciative of the guidance provided by Dr. Daniel E. Perea of Environmental Molecular Sciences Laboratory, Pacific Northwest National Laboratory, 902 Battelle Blvd, Richland, WA 99352. This report was prepared as an account of work sponsored by an agency of the United States Government. Neither the United States Government nor any agency thereof, nor any of their employees, makes any warranty, express or implied, or assumes any legal liability or responsibility for the accuracy, completeness, or usefulness of any information, apparatus, product, or process disclosed, or represents that its use would not infringe privately owned rights. Reference herein to any specific commercial product, process, or service by trade name, trademark, manufacturer, or otherwise does not necessarily constitute or imply its endorsement, recommendation, or favoring by the United States Government or any agency thereof. The views and opinions of authors expressed herein do not necessarily state or reflect those of the United States Government or any agency thereof.

REFERENCES

1. R.J. Allam: NET Power's CO₂ cycle: the breakthrough that CCS needs, www.modernpowersystems.com/features/, 2013.
2. R. Dennis: *EPRI International Conference on Corrosion in Power Plants*, Palo Alto, CA, USA, 2015, pp. 2-136-132-153.
3. B.K. Paul: *Micro Energy and Chemical Systems (MECS) and Multiscale Fabrication*, Springer, Berlin, 2006, pp. 299-355.
4. L.M. Pike and S.K. Srivastava: *Adv. Mater. Res.*, 2011, vol. 278, pp. 327-32.
5. H.M. Tawancy, D.L. Klarstrom, and M.F. Rothman: *JOM*, 1984, vol. 36, pp. 58-62.
6. D. Klarstrom, H. Tawancy, D. Fluck, and M. Rothman: *ASME 1984 International Gas Turbine Conference and Exhibit*, American Society of Mechanical Engineers, 1984, pp. V005T11A003-V005-T11A003.
7. M.A. Arafin, M. Medraj, D.P. Turner, and P. Bocher: *Mater. Chem. Phys.*, 2007, vol. 106, pp. 109-19.
8. M.A. Arafin, M. Medraj, D.P. Turner, and P. Bocher: *Mater. Sci. Eng. A*, 2007, vol. 447, pp. 125-33.
9. A. Egbewande, C. Chukwukaeme, and O. Ojo: *Mater. Charact.*, 2008, vol. 59, pp. 1051-58.
10. A. Ekrami, S. Moeinifar, and A.H. Kokabi: *Mater. Sci. Eng. A*, 2007, vol. 456, pp. 93-98.
11. O.A. Idowu, N.L. Richards, and M.C. Chaturvedi: *Mater. Sci. Eng. A*, 2005, vol. 397, pp. 98-112.
12. Y. Natsume, K. Ohsasa, and T. Narita: *Mater. Trans., JIM*, 2003, vol.44, pp. 819-823.
13. W. Gale and E. Wallach: *Metall. Trans. A*, 1991, vol. 22A, pp. 2451-2457.
14. D.M. Jacobson and G. Humpston: *Principles of Brazing*, ASM International, 2005.
15. F. Jalilian, M. Jahazi, and R.A.L. Drew: *Mater. Sci. Eng. A*, 2006, vol. 423, pp. 269-81.
16. M. Pouranvari, A. Ekrami, and A.H. Kokabi: *J. Alloys Compd.*, 2009, vol. 469, pp. 270-75.
17. G.O. Cook and C.D. Sorensen: *J. Mater. Sci.*, 2011, vol. 46, pp. 5305-23.
18. A. Ghoneim and O. Ojo: *Mater. Charact.*, 2011, vol. 62, pp. 1-7.
19. O.A. Ojo, N.L. Richards, and M.C. Chaturvedi: *Sci. Technol. Weld. Join.*, 2004, vol. 9, pp. 532-40.
20. R. Bakhtiari and A. Ekrami: *Mater. Des.*, 2012, vol. 40, pp. 130-37.
21. T.C. Illingworth, I.O. Golosnoy, and T.W. Clyne: *Mater. Sci. Eng. A*, 2007, vols. 445-446, pp. 493-500.
22. N.S. Bosco and F.W. Zok: *Acta Mater.*, 2004, vol. 52, pp. 2965-72.
23. N.S. Bosco and F.W. Zok: *Acta Mater.*, 2005, vol. 53, pp. 2019-27.
24. M. Tseng, D. Williams, K. Soni, and R. Levi-Setti: *J. Mater. Sci.*, 1999, vol. 34, pp. 5187-97.
25. M. Kapoor, Ö. Doğan, K. Rozman, J. Hawk, A. Wilson, T. L'Estrange, V. Narayanan: *Proceedings of the 5th International Symposium on Supercritical CO₂ Power Cycles*, San Antonio, Texas, 2016.
26. J.-O. Andersson, T. Helander, L. Höglund, P. Shi, and B. Sundman: *Calphad*, 2002, vol. 26, pp. 273-312.
27. E.E. Underwood: *Quantitative Stereology*, Addison-Wesley, Massachusetts, 1970.
28. ASTM standard E8: *Standard Test Methods for Tension Testing of Metallic Materials*, ASTM International, West Conshohocken, PA, 2013.
29. H. Chuang, J. Yu, M. Kuo, H. Tong, and C. Kao: *Scripta Mater.*, 2012, vol. 66, pp. 171-74.
30. A. Lis and C. Leinenbach: *J. Electron. Mater.*, 2015, vol. 44, pp. 4576-88.
31. A. Sakamoto: *Weld. J.*, 1989, vol. 69, pp. 63-71.
32. M.K. Miller: *Atom Probe Tomography: Analysis at the Atomic Level*, Springer, 2012.
33. D.J. Larson, T.J. Prosa, R.M. Ulfig, B.P. Geiser, and T.F. Kelly: *Local Electrode Atom Probe Tomography*, Springer, New York, 2013.
34. W. Cao and R. Kennedy: *Superalloys 718, 625, 706 and Various Derivatives*, 1994, pp. 463-77.
35. M. Wang, J. Du, Q. Deng, Z. Tian, and J. Zhu: *Mater. Sci. Eng. A*, 2015, vol. 626, pp. 382-89.
36. J. Goldstein, D.E. Newbury, P. Echlin, D.C. Joy, A.D. Romig Jr, C.E. Lyman, C. Fiori, and E. Lifshin: *Scanning electron microscopy and X-ray microanalysis: a text for biologists, materials scientists, and geologists*, Springer, 2012.
37. T.H. Courtney: *Mechanical Behavior of Materials*, Waveland Press, Long Grove, 2005.